Journal of Magnetic Resonance 202 (2010) 180–189

Contents lists available at ScienceDirect

Journal of Magnetic Resonance

journal homepage: www.elsevier.com/locate/jmr

Slice profile effects in 2D slice-selective MRI of hyperpolarized nuclei

Martin H. Deppe, Kevin Teh, Juan Parra-Robles, Kuan J. Lee [1], Jim M. Wild *

Academic Radiology, University of Sheffield, C Floor Royal Hallamshire Hospital, Glossop Road, Sheffield S10 2JF, United Kingdom

ARTICLE INFO

Article history:
Received 11 May 2009
Revised 10 November 2009
Available online 13 November 2009

Keywords:
MRI
Hyperpolarization
3He
Slice profiles
2D gradient echo

ABSTRACT

This work explores slice profile effects in 2D slice-selective gradient-echo MRI of hyperpolarized nuclei. Two different sequences were investigated: a Spoiled Gradient Echo sequence with variable flip angle (SPGR-VFA) and a balanced Steady-State Free Precession (SSFP) sequence. It is shown that in SPGR-VFA the distribution of flip angles across the slice present in any realistically shaped radiofrequency (RF) pulse leads to large excess signal from the slice edges in later RF views, which results in an undesired non-constant total transverse magnetization, potentially exceeding the initial value by almost 300% for the last RF pulse. A method to reduce this unwanted effect is demonstrated, based on dynamic scaling of the slice selection gradient. SSFP sequences with small to moderate flip angles (<40°) are also shown to preserve the slice profile better than the most commonly used SPGR sequence with constant flip angle (SPGR-CFA). For higher flip angles, the slice profile in SSFP evolves in a manner similar to SPGR-CFA, with depletion of polarization in the center of the slice.

1. Introduction

Gradient recalled echo sequences are the most commonly used pulse sequences in MRI of hyperpolarized nuclei. While sequences based on non-Cartesian *k*-space trajectories [1–3] promise faster acquisitions and efficient use of available polarization due to non-uniform *k*-space sampling, 2D and 3D Cartesian sequences remain popular as they are robust, readily implemented and images are easily reconstructed.

The most widely used sequence is the 2D Spoiled Gradient Echo (SPGR) sequence, also known as Fast Low-Angle Shot (FLASH) [4]. Alternatively, balanced Steady-State Free Precession sequences (SSFP, TrueFISP, FIESTA) [5–7] are emerging in hyperpolarized noble gas imaging [8], as they are able to provide a higher signal-to-noise ratio (SNR) through recycling of available polarization, albeit at the risk of steady-state banding artifacts in regions of low B_0 homogeneity.

Hyperpolarized nuclei are by definition in a non-equilibrium state, and longitudinal relaxation does not lead to a recovery of polarization between radiofrequency (RF) pulses. Instead, hyperpolarization decays exponentially with the time constant T_1 towards thermal equilibrium, and the remaining thermal polarization can be considered negligible compared to the hyperpolarized state. This T_1 decay and irradiation with RF leads to a steady depletion of polarization in the excited sample volume.

Fig. 1 shows the effect this steady depletion of polarization has on the evolution of the slice profile between RF pulses (Fig. 1a), and the effective *k*-space filter (Fig. 1b) for a 2D SPGR sequence with constant flip angle (SPGR-CFA). The optimum flip angle that maximizes SNR can be derived analytically for SPGR-CFA with sequential phase encoding [9], and is about 7° for 128 phase encode steps. The slice profile evolution in Fig. 1 was obtained experimentally using this optimal flip angle. A reduction in flip angle would improve the slice profile and the effective *k*-space filter at the expense of image SNR.

The non-constant *k*-space filter leads to image blurring. This effect is already known in hyperpolarized MRI [9], and the data in Fig. 1 are shown here for reference. Depletion of polarization can be countered by the use of progressively increasing flip angles in SPGR imaging, effectively yielding a constant transverse magnetization after each RF pulse. This approach is used in ^{1}H imaging at short TR [10], but is particularly useful in hyperpolarized MRI [11] as the optimal flip angle progression can be calculated analytically. In theory, the constant transverse magnetization imparts a constant *k*-space filter and thus reduces image blurring. Additionally, by employing a flip angle progression scheme that results in a flip angle of 90° for the last pulse, the finite polarization available is used completely and therefore efficiently.

The aim of this work was to evaluate slice profile evolution and *k*-space filtering in slice-selective 2D MRI for hyperpolarized nuclei, using an SPGR sequence with variable flip angle (SPGR-VFA) and a balanced SSFP sequence for imaging of hyperpolarized ^{3}He. It is shown that for realistic RF pulse shapes the progressive flip angle scheme in SPGR-VFA leads to unwanted slice profile distortion for later pulses. Different solutions to counter this effect are

* Corresponding author. Fax: +44 114 271 1714.
E-mail address: j.m.wild@shef.ac.uk (J.M. Wild).
[1] Present address: Medizin Physik, Uniklinik Freiburg, RDiag Hugstetterstr. 55, D-79106 Freiburg, Germany.

1090-7807/$ - see front matter © 2009 Elsevier Inc. All rights reserved.
doi:10.1016/j.jmr.2009.11.003

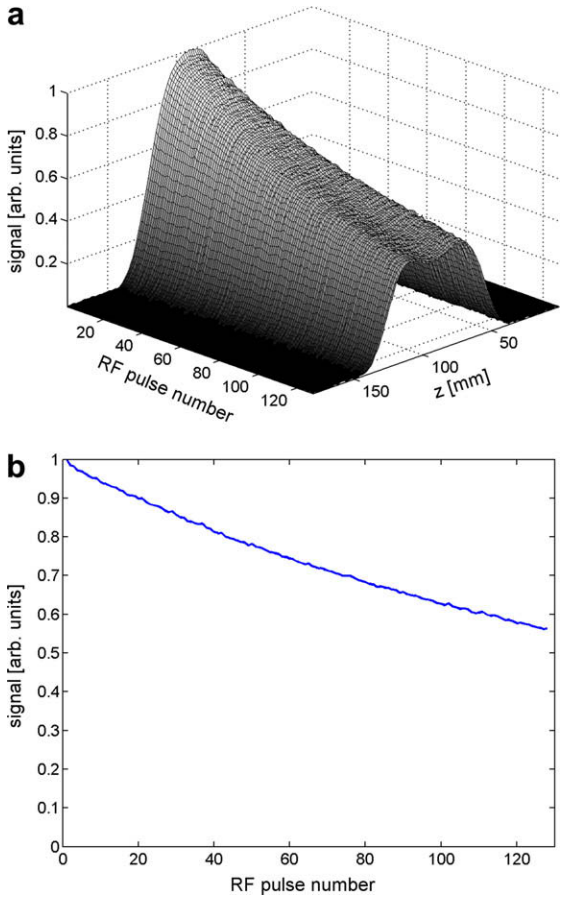

Fig. 1. (a) Experimentally obtained evolution of the slice profile in SPGR imaging of hyperpolarized nuclei employing a constant flip angle (SPGR-CFA). The FOV is 18 cm, the slice thickness 6 cm and the flip angle is 7°. (b) The effective *k*-space filter in the phase encode direction resulting from integration of signal across the slice, assuming sequential phase encoding.

discussed, and an easily implemented correction method using dynamic scaling of the slice selection gradient is proposed.

Additionally, slice profile effects were investigated for a 2D SSFP sequence for a range of flip angles, and results indicate that for equivalent flip angles the slice profile is better conserved in SSFP than in SPGR-CFA.

2. Theory

For SPGR-VFA of hyperpolarized media the ideal flip angle progression can be expressed analytically [11], as T_1 relaxation can usually be neglected on the time scale of the imaging sequence:

$$\alpha_n = \arctan\left(\frac{1}{\sqrt{N-n}}\right) \tag{1}$$

where N is the total number of RF pulses and α_n is the flip angle for the nth RF pulse. This progression scheme ideally leads to a constant transverse magnetization after each pulse. For a realistic slice-selective experiment, Eq. (1) cannot be satisfied over the whole slice because of the distribution of effective flip angles over the slice excitation profile.

Fig. 2 shows the geometry used here for the slice profile measurements. Note that the ^{3}He phantom extends well beyond the nominal boundary of the measured slice as defined by the FWHM. This is necessary to highlight the flip angle inhomogeneity across the slice and represents a realistic situation for 2D in vivo imaging in a continuous object. Additionally, this minimizes potential

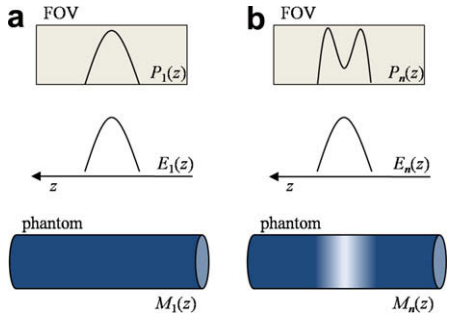

Fig. 2. From bottom to top: The distribution of magnetization within the phantom $M_n(z)$, the slice excitation profile $E_n(z)$, and the observed slice profile $P_n(z)$ within the FOV, (a) for the first RF pulse ($n = 1$) and (b) for a later RF pulse ($n > 1$). Before the first RF excitation, $M_1(z)$ is homogeneous over the whole phantom, and the observed profile $P_1(z)$ mirrors the excitation profile $E_1(z)$. For subsequent RF pulses, magnetization is gradually depleted by RF pulses, leading to a reduced $M_n(z)$ at the slice location. As a consequence, the observed profile $P_n(z) = E_n(z) \cdot M_n(z)$ is distorted.

confounding effects due to diffusion restriction close to the edges (see Section 5).

In a simple model, the observed slice profile after the nth RF pulse $P_n(z)$, equal to the transverse magnetization, $M_{xy}(z)$, can be expressed as the product of the excitation profile of the RF pulse $E_n(z)$ and the underlying spatial distribution of longitudinal magnetization $M_n(z)$:

$$P_n(z) = E_n(z) \cdot M_n(z) \tag{2}$$

$P_n(z)$ is the slice profile observed experimentally. $E_n(z)$ is equivalent to the observed slice profile if the underlying longitudinal magnetization is distributed uniformly. $E_n(z)$ depends on the RF pulse shape and the flip angle, but also includes the effect of imperfect RF coil homogeneity. Essentially it is the actual excitation profile of the RF pulse as experienced by the spins in image space.

As no recovery of polarization occurs in hyperpolarized MRI, the distribution of longitudinal magnetization $M_n(z)$ depends on the RF pulse number n. Fig. 2a depicts the case of $n = 1$, where $M_n(z)$ is still constant in space. Fig. 2b shows the situation at a later stage; here, previous RF pulses have depleted the magnetization at the slice location, and the observed slice profile $P_n(z)$ is distorted, although the excitation profile $E_n(z)$ remains unchanged.

Ideally, the observed slice profile for all pulses $P_n(z)$ would be identical to the excitation profile of the first pulse $E_1(z) = P_1(z)$. The shape of the excitation profile $E_n(z)$ depends on the RF pulse shape, and can be regarded as independent of flip angle as long as the latter is small (<90°). In that case, the excitation profile can be approximated as the Fourier transform of the temporal envelope of the RF pulse. Hence, if this small flip angle approximation is valid and the RF pulse shape is not changed during the experiment, the excitation profiles differ only by a scaling factor proportional to the RF pulse amplitude and independent of z, leading to

$$E_n(z) \propto E_1(z) = P_1(z) \tag{3}$$

A corrected excitation profile $E_{corr,n}(z)$ can be proposed which would meet the condition

$$P_n(z) = P_1(z) = E_{corr,n}(z) \cdot M_n(z) \tag{4}$$

From Eqs. (2)–(4) it follows that

$$E_{corr,n}(z) \propto \frac{P_1(z)^2}{P_n(z)} \tag{5}$$

Thus the corrected excitation profile $E_{corr,n}(z)$ can be determined empirically from the slice profiles $P_n(z)$ observed with the uncorrected excitation profile, except for a scaling factor related to the

RF pulse amplitude As the correction mechanism proposed in Section 4 relies solely on the full width at half maximum (FWHM) of $E_{corr,n}(z)$, this scaling factor can from here on be neglected.

Note that this calculation is done entirely in spatial coordinates, as only the spatial excitation profile of the RF pulse has been investigated, not its time envelope. As long as the corrected excitation profiles $E_{corr,n}(z)$ are based on actually observed uncorrected profiles, additional effects of polarization mixing due to diffusion of gas in and out of the excited slice, which lead to broadened slice profiles [12], are intrinsically considered in this analysis.

A method based on Shinnar–Le Roux transformation [13] to compensate for RF depletion has been proposed by implementing a view dependent modification of the RF pulse shape [14]. In Section 4, it will be shown that a purely spatial modulation by scaling of the slice gradient amplitude also yields satisfactory results.

3. Experimental

Measurements were conducted on a GE 1.5T Signa HDx scanner (GE, Milwaukee, WI, USA), using a home-built linear Birdcage coil tuned to the ^{3}He resonance frequency of 48.63 MHz. The coil has a diameter of 15 cm and a length of 19 cm, and is surrounded by an RF shield of 22 cm diameter. A B_1 map of the coil is given in Ref. [15]. ^{3}He was polarized to ~25% using a prototype Rubidium spin-exchange polarizer (GE, Milwaukee, WI, USA). To image slice profiles a cylindrical 400 ml glass phantom filled with 100 ml hyperpolarized ^{3}He and 300 ml N_2 was used. Slice profiles were obtained by placing the read and slice gradients on the same axis and nulling the phase encode gradients for each encoding step (view).

Imaging parameters for SPGR sequences were a 128 × 128 matrix, a receiver bandwidth of 31.25 kHz, a FOV of 18 cm and a slice thickness of 6 cm. The relatively small FOV and thick slice were chosen to resolve the slice profile well. Sequence timing was TE = 4.2 ms and TR = 8.7 ms. For the SSFP sequence, receiver bandwidth and FOV were increased to 250 kHz and 48 cm, respectively, while maintaining a 128 × 128 matrix and a 6 cm slice thickness. The timing was TE = 4.2 ms and TR = 2TE = 8.4 ms. In SSFP imaging the magnetization was catalyzed by a single $\alpha/2 - TR/2$ start-up phase. The long echo times for both SPGR and SSFP are a consequence of accommodating both slice and read gradient waveforms on the same axis.

Before SSFP imaging the magnet was shimmed manually to ~0.2 ppm FWHM of the main spectral peak observed. A small second resonance amounting to less than 5% of the total intensity was observed about 2 ppm up-field, which is attributed to the neck of the phantom used for filling. During the shimming process the main peak was brought on resonance, and all SSFP profiles presented here were acquired with RF excitation at this frequency.

Four different RF pulses were used for the experiments with the SPGR sequence: a symmetric sinc pulse apodized with a Hamming window, truncated either at the second, third or fourth zero-crossing. These pulses are designated $sinc_1$, $sinc_2$ and $sinc_3$, respectively. The fourth pulse was a symmetric Gaussian. For the SSFP sequence only the Gaussian pulse was used. The transmit bandwidths were 5 kHz for $sinc_1$, 10 kHz for $sinc_2$, 15 kHz for $sinc_3$, 4.0 kHz for the Gaussian pulse in SPGR and 4.163 kHz for the Gaussian pulse in SSFP.

Prior to imaging, the flip angle was calibrated by placing a small sphere containing hyperpolarized ^{3}He at the center of the RF coil, and monitoring the depletion of signal using a non-slice-selective pulse-acquire sequence with constant flip angle and spoiling before each RF pulse. The signal decays according to

$$S_n = S_1 \cdot (\cos\alpha)^{(n-1)} \tag{6}$$

Here, S_n is the signal after the nth RF pulse, and α is the flip angle. A fit of Eq. (6) to the resulting signal amplitudes allows extraction of α. The flip angle was calibrated separately for each RF pulse shape used in this work.

To assess the possibility of using simulated rather than measured slice profiles as $P_1(z)$ and $P_n(z)$ for determination of $E_{corr,n}(z)$ via Eq. (5), SPGR-VFA slice profiles were simulated in MATLAB (MathWorks, Natick, MA, USA), using matrix multiplication methods based on the Bloch equations [8] assuming the low flip angle approximation whereby the slice profile is given by the Fourier transform of the RF pulse envelope. The simulations used the actual Gaussian RF pulse shape as stored on the scanner. Simulation input parameters were: TE = 4.2 ms, TR = 8.7 ms, $T_2^* = 27.5$ ms, $T_1 = 1200$ s.

All slice profile data sets shown in this work were divided by the amplitude of the first profile. This normalizes the peak of the first profile to unity amplitude and maintains the relative amplitudes of subsequent profiles.

4. Results

4.1. SPGR-VFA

Fig. 3 shows slice profiles (a–d) and k-space filters (e) measured for a 2D SPGR-VFA sequence for four different RF pulse shapes and with flip angle progression according to Eq. (1). For the number of RF pulses used ($N = 128$), this corresponds to a flip angle evolving from 5° for the first pulse to 90° for the last. It can be seen that Eq. (1) is satisfied well in the center of the slice resulting in a constant signal with increasing n at $z = 0$, which is an improvement over the depletion seen in SPGR-CFA (Fig. 1a).

Towards the end of the sequence, however, the lower effective flip angle at the slice edges leads to a distortion of the slice profile, with large excess signal lobes arising at the edges. This is a consequence of insufficient depletion of polarization during the earlier pulses.

Comparing the different pulse shapes, sinc pulses with a larger time–bandwidth product (corresponding to a larger number of zero crossings) inherently have a flatter flip angle distribution across the slice, and hence are able to maintain the slice profile better. On the other hand they have increased sidebands, which start to become more prominent at the final RF view where the flip angle is 90°.

Usually in thermally polarized experiments, the sidebands of sinc pulses are still considered negligible at a flip angle of 90°. In the present experiment, however, the situation is somewhat different. As the 90° sidebands extend beyond the nominal slice, they excite areas which have not been depleted at all by previous RF pulses. Hence the large excess in polarization outside of the slice in combination with the relatively small (but not negligible) flip angles arising from the sidebands can result in the fact that most of the signal for the final RF view arises from outside of the actual slice. This effect can be seen in Fig. 3b and c.

The k-space filters resulting from integration of signal across the slice are shown in Fig. 3e. As expected, sinc pulses with a larger time–bandwidth product perform best in the earlier phase of the imaging sequence. Almost no difference in k-space filter is observed between $sinc_2$ and $sinc_3$, both of which deviate from a flat response by 10% after the 105th RF pulse. For $sinc_1$ the same 10% deviation is observed after the 69th pulse, and after the 53rd pulse for the Gaussian shape. For the latter, the signal enhancement of the last RF pulse amounts to almost 300%.

4.1.1. Slice profile correction from empirical data

The data shown in Fig. 3 were used to calculate the ideal excitation profiles according to Eq. (5). Fig. 4a depicts the excitation

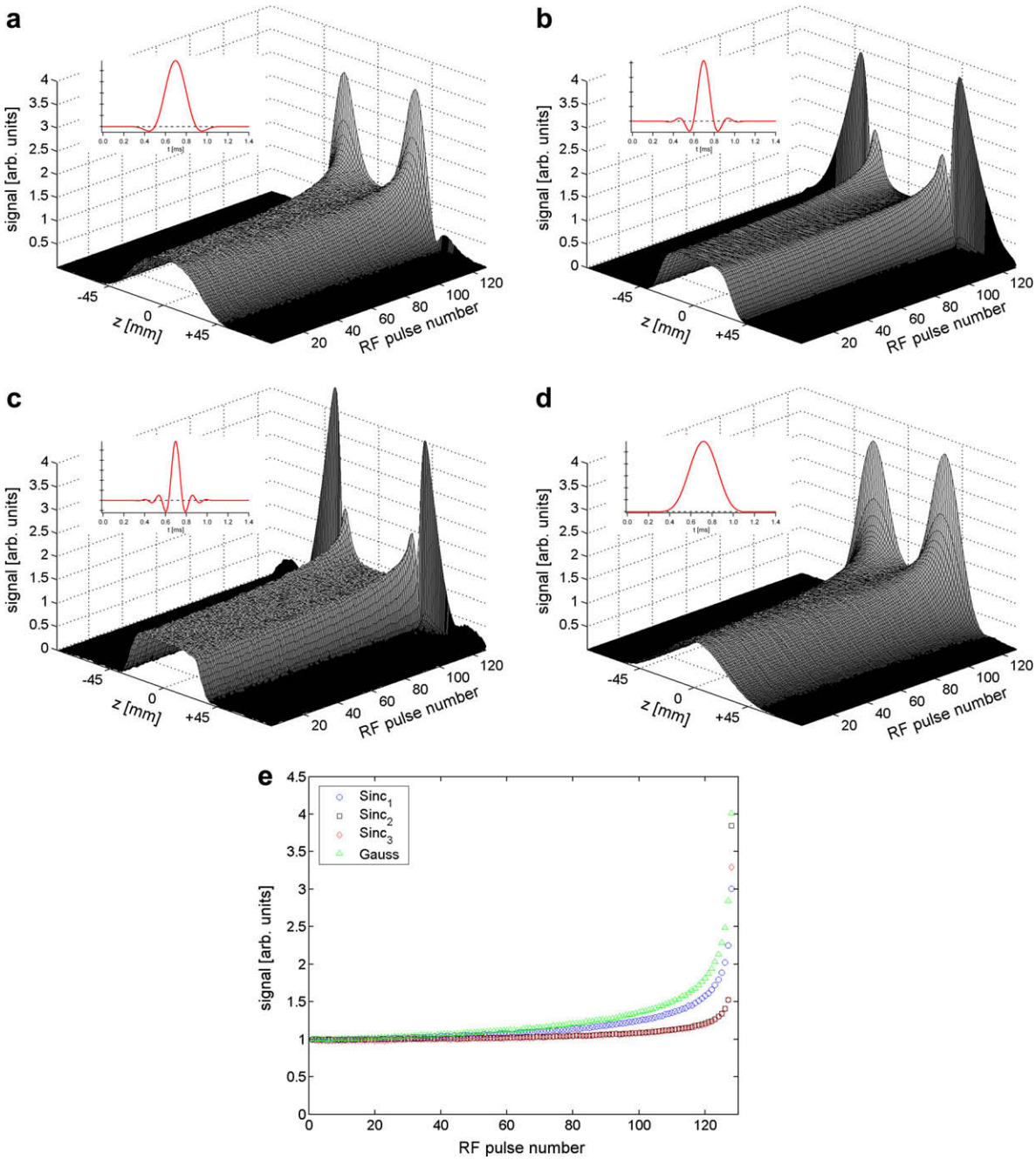

Fig. 3. Evolution of the slice profile with SPGR-VFA of hyperpolarized ^{3}He observed experimentally, for different RF pulse shapes: (a) sinc_1, (b) sinc_2, (c) sinc_3 and (d) Gaussian. The RF pulse shapes in the temporal domain are given in the insets. (e) The effective k-space filters in the phase encode direction obtained from integration of the signal across the slice.

profiles $E_1(z) = E_{corr,1}(z)$ and $E_{corr,128}(z)$ for the case of the Gaussian RF pulse. The shape of $E_{corr,n}(z)$ does vary with n, and the ideal excitation profile could be realized by dynamic shaping of the RF pulse [14]. The main variation in excitation profile shape, however, is via its width. In Fig. 4a, a Gaussian excitation profile with identical FWHM to $E_{corr,128}(z)$ is plotted, and it can be seen that although it differs from the ideal profile, this difference is quite small.

This insight leads to a simpler approach to slice profile correction. Instead of using a different RF pulse shape for each n, the slice gradient is scaled while maintaining the same RF pulse shape, to yield an excitation profile of identical FWHM to the ideal excitation profile $E_{corr,n}(z)$. As the slice thickness is inversely proportional to the slice gradient amplitude, the scaling factor is proportional to the inverse of the FWHM of $E_{corr,n}(z)$. Fig. 4b shows the correction factor function for the different RF pulses as obtained from the data in Fig. 3.

To obtain a smooth correction curve the following empirical function was fitted to the correction factors obtained from the inverse FWHM:

$$F(n) = A + \frac{B}{(n-n_0)} + \frac{C}{(n-n_0)^2} + \frac{D}{(n-n_0)^3} \tag{7}$$

$F(n)$ is the correction factor by which the slice selection gradient is to be scaled for the nth RF pulse. A, B, C, D and n_0 are fitting parameters, and their values for the different RF pulses are given

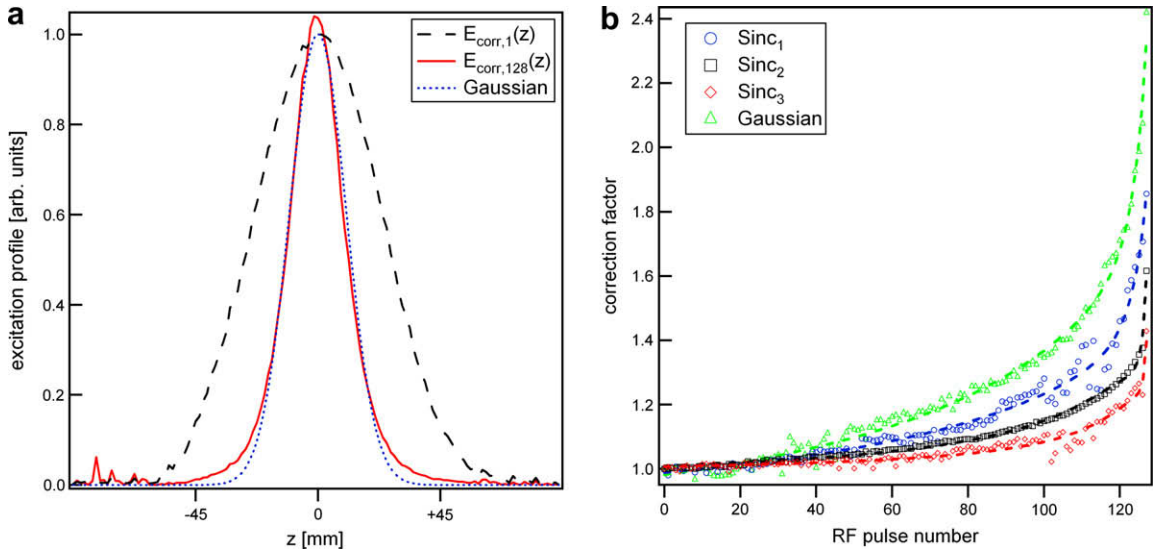

Fig. 4. (a) The corrected excitation profiles $E_{corr,1}(z)$ and $E_{corr,128}(z)$ calculated from the data shown in Fig. 3(d) using Eq. (5), and compared to a Gaussian. (b) The correction factors derived from FWHM^{-1} of $E_{corr,n}(z)$ for the different pulse shapes. Dashed lines in (b) are the best fits in a least squares sense, using Eq. (7) and the parameter values given in Table 1.

in Table 1. The best fits in a least squares sense are also depicted in Fig. 4b. The inverse polynomial form was chosen instead of a normal polynomial to better represent the divergence for later RF pulses.

Fig. 5 shows the resulting slice profile measurements from a SPGR-VFA sequence, with scaling of the slice selection gradient amplitude according to the correction factors shown in Fig. 4b. Slice profile distortion has been reduced for all four RF pulse shapes (Fig. 5a–d). The effect of the correction mechanism is most pronounced for the $sinc_1$ (Fig. 5a) and Gaussian (Fig. 5d) pulse shapes, which performed worst without correction (Fig. 3).

While the shapes of the observed profiles in the later pulses still deviate from the original excitation profiles, the imposed *k*-space filter has been significantly improved (Fig. 5e). The signal integrated over the profile remains within ±5% of the starting value for the first 127 RF pulses for $sinc_1$ and Gaussian, and within ±12% for $sinc_2$ and $sinc_3$. Remaining deviations from a flat response are attributed to the emergence of sidebands in the later RF pulses (which are not accounted for in the derivation leading to Eq. (5), and which are more significant for pulses with a larger time–bandwidth product) and possible errors in phantom placement between uncorrected and corrected measurement (as occasionally the phantom had to be refilled).

4.1.2. Slice profile correction from simulations

Slice gradient scaling according to correction factors determined from uncorrected profiles requires an additional measurement. Fig. 6 assesses the possibility of replacing this preparation measurement with simulated data requiring only knowledge of the RF pulse shape. Fig. 6a shows the slice profile evolution observed experimentally for the Gaussian RF pulse, while Fig. 6b shows profiles simulated with matrix multiplication methods [8].

Table 1
The fitting parameters for the correction factor in Eq. 7, resulting in the correction factors shown in Fig. 4b.

Pulse shape	*A*	*B*	*C*	*D*	n_0
$sinc_1$	0.707	−45.32	−975.26	−9825.6	141.84
$sinc_2$	0.947	−8.92	−84.88	−301.74	132.4
$sinc_3$	0.949	−8.76	−178.3	−2128.7	142.03
Gaussian	0.803	−31.38	−746.18	−8365.7	143.24

The actual RF pulse envelope as obtained from the scanner was used as input for the simulations. Small deviations between experimental data and simulation are due to the fact that the effects of B_1 inhomogeneity and diffusion are not accounted for in the simulations.

Figs. 6c and d show the profiles observed experimentally with slice gradient scaling, with the correction factors obtained from experimental data and simulations, respectively. Qualitatively no great difference is observed between the two approaches. Fig. 6e shows the correction factors obtained from both methods, and it can be seen that the simulated data results in larger gradient scaling throughout. This translates directly to the effective *k*-space filters shown in Fig. 6f. The data obtained with correction from experimental data deviates to higher signal for later RF pulses, while the data obtained with correction from simulation appears to deviate to lower signal initially, curving upwards only for the last pulses. This is a consequence of overestimated correction factors obtained from simulation. In both cases, however, the effective *k*-space filter has been greatly improved by slice gradient scaling.

4.2. SSFP

In SSFP imaging, dephasing of transverse magnetization due to diffusion along field gradients plays a somewhat more important role than in SPGR imaging, because it attenuates the desired coherence between gradient echoes. The effective transverse relaxation time $T_{2,eff}$ is given by [16]:

$$T_{2,eff} = \frac{\mathrm{TE}}{b(\mathrm{TE}) \cdot D + \mathrm{TE}/T_2} \tag{8}$$

Here, TE is the echo time, *D* is the diffusion coefficient, T_2 is the upper limit for the transverse relaxation time as measured by a CPMG sequence, and b(TE) is the *b*-factor related to the gradient waveform [8]. According to Eq. (8), large diffusion dephasing due the free diffusion of the gas in the strong gradients leads to a short $T_{2,eff}$. This effectively converts a SSFP sequence into a SPGR sequence, as the read gradient works as a spoiler and prevents recycling of magnetization. Hence, in order to achieve true SSFP conditions, the field of view (FOV) and receiver bandwidth were increased for the SSFP experiments, which is consistent with realistic parameters for in vivo imaging.

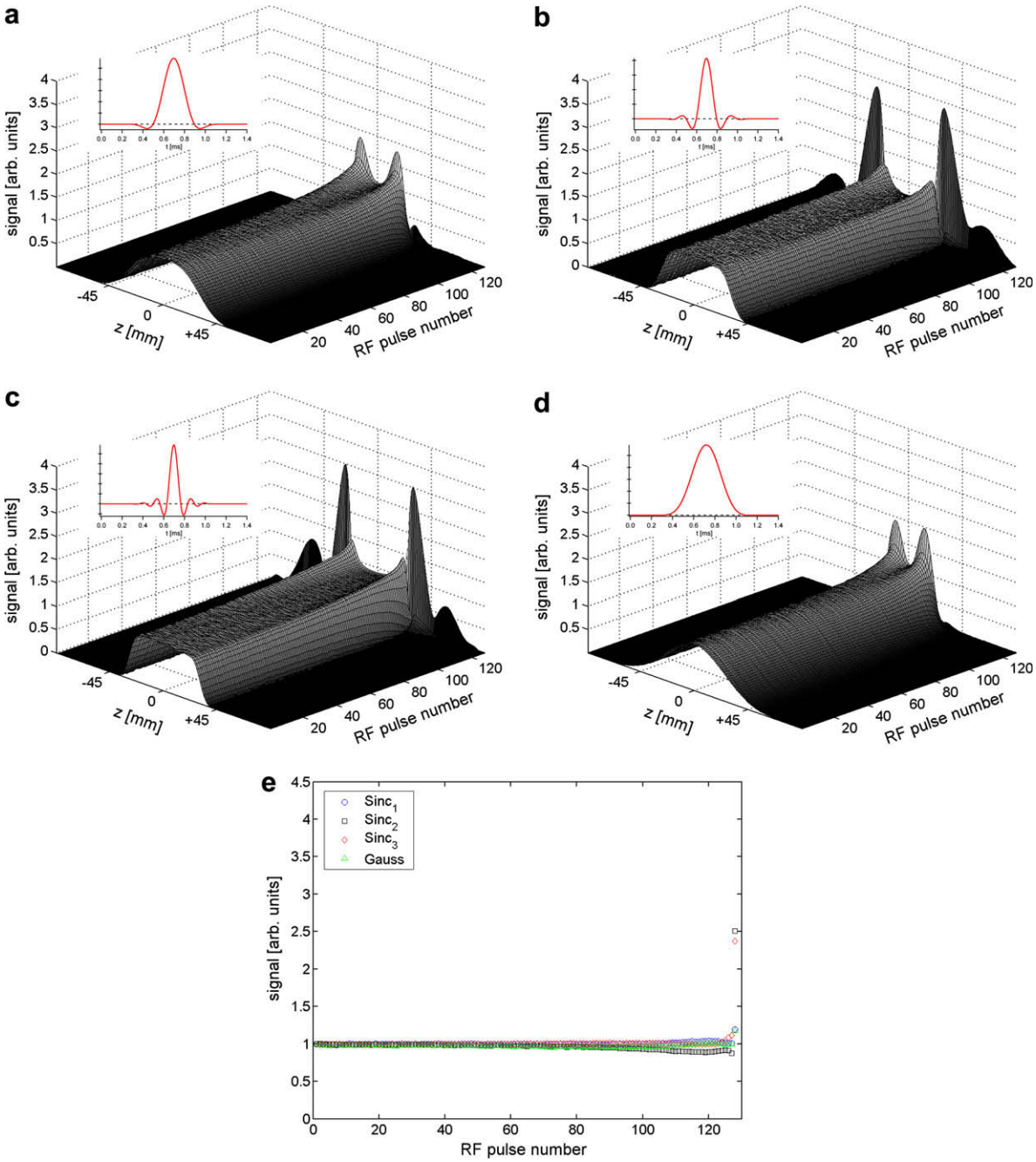

Fig. 5. Experimentally observed evolution of slice profiles in SPGR-VFA corrected by slice gradient scaling, for the different RF pulse shapes: (a) $sinc_1$, (b) $sinc_2$, (c) $sinc_3$, (d) Gaussian. Scaling factors were derived from the experimental data shown in Fig. 3. (e) The resulting effective *k*-space filters. Note that for comparison all axes are scaled identically to those in Fig. 3.

Fig. 7a–c show the evolution of slice profiles obtained with a SSFP sequence for a range of flip angles. For comparison, the case of SPGR-CFA with $\alpha = 7^\circ$ using the same FOV is shown in Fig. 7d. Note that, because of the absence of spoiling and due to phase cycling of ±180° of the transmit pulse, a SSFP flip angle of α leads to the same transverse magnetization as a SPGR sequence with a flip angle of $\alpha/2$ when relaxation is neglected [7]; hence the cases shown in Fig. 7a and d yield comparable signal, while for Fig. 7b and c the detected signal is higher by virtue of a larger flip angle. Due to the rescaling for comparison of the slice profiles, this improvement in absolute signal with increased flip angle is not apparent in Fig. 7.

From Fig. 7 it can be seen that a balanced SSFP sequence conserves the slice profile better than the standard SPGR-CFA sequence for a comparable flip angle. In SPGR-CFA with 128 phase encode views, a flip angle of 7° yields optimal SNR, and the corresponding slice profile evolution with the known effect of RF depletion is shown in Fig. 7d. In SSFP, a flip angle of 14° leads to the same transverse magnetization, while the slice profile is better maintained, exhibiting no depletion in the slice center (Fig. 7a). RF depletion only becomes significant at higher flip angles, as shown in Fig. 7b and c.

Nevertheless, unwanted slice profile distortion is observed for the first ~20 RF pulses in the SSFP sequence, which is a consequence of imperfect catalyzing of the equilibrium magnetization prior to acquisition. In this work a single $\alpha/2 - TR/2$ start-up period was used, which assumes all spins to be exactly on resonance [17]. In practice this ideal condition is never reached completely, and

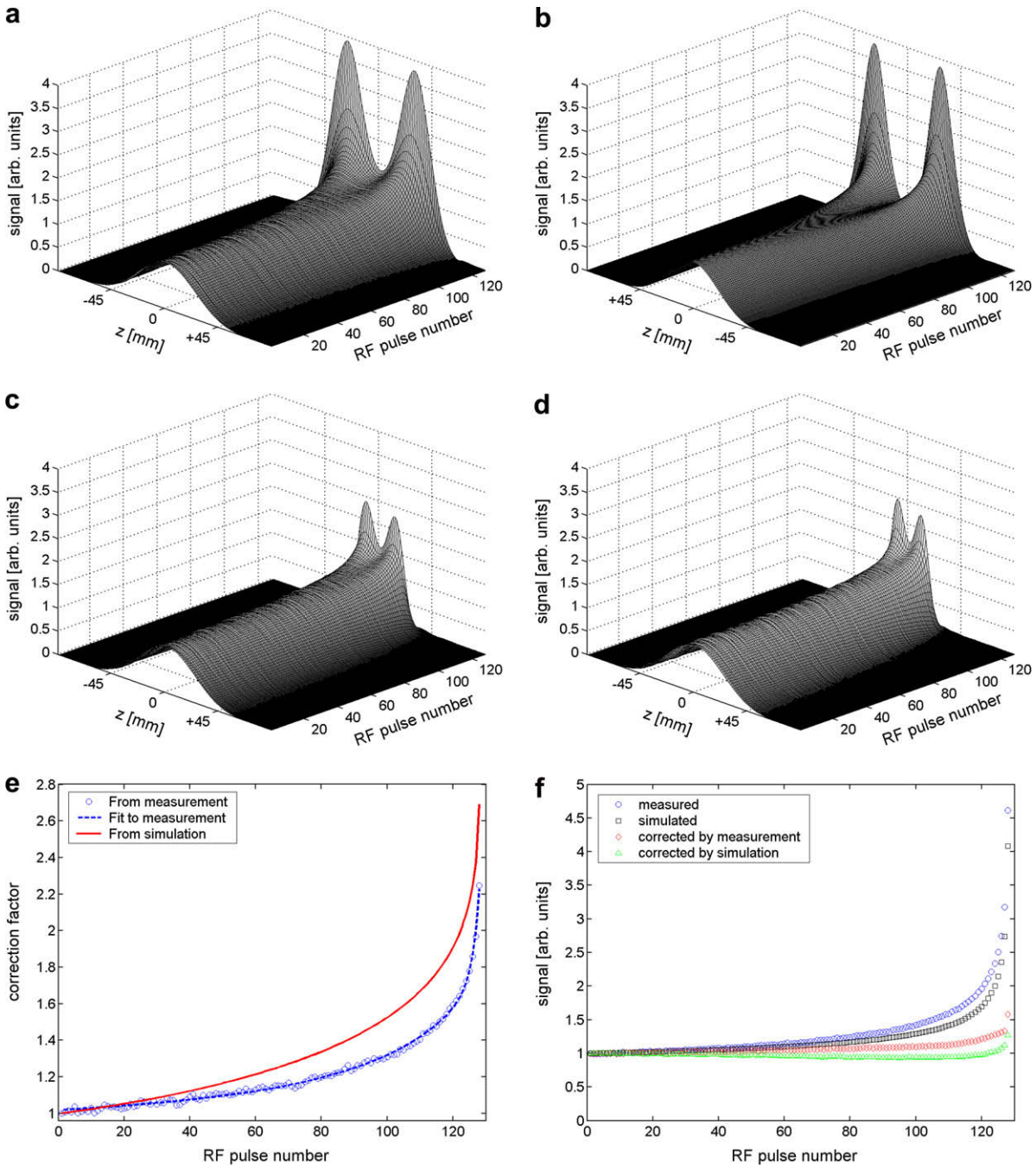

Fig. 6. Comparison between slice gradient scaling factors obtained from previous experimental data and from simulations. (a) Experimentally observed slice profiles for SPGR-VFA obtained with the Gaussian RF pulse without slice gradient scaling. (b) Slice profiles simulated from knowledge of the RF pulse shape. (c) Measured profiles with the correction factor derived from the experimental data in (a). (d) Measured profiles with the correction factor derived from the simulated data in (b). (e) The correction factors obtained from the measurement in (a) and the simulation in (b). (f) The resulting *k*-space filters from the slice profiles shown in (a–d).

off-resonance spins contribute to the signal during the first few RF views, until they have dephased and only on-resonance spin coherences remain.

5. Discussion

This work has shown that slice profile effects in 2D SPGR-VFA of hyperpolarized nuclei lead to an overall signal response that diverges with RF pulse number *n*, resulting in a non-uniform *k*-space filter in the phase encode direction. This is a consequence of variation of the flip angle across the slice profile, making it impossible to satisfy the optimum SPGR-VFA condition in Eq. (1) at every location. Here, the flip angle has been calibrated so that Eq. (1) is fulfilled at the slice center. This results in the desired flat signal response in the middle of the slice, but at the same time leads to insufficient depletion of polarization and subsequent excess signal at the slice edges.

The data presented here show that automatic calculations of flip angles in SPGR-VFA according to Eq. (1) can lead to slice profile distortions and excess signal, in the worst case amounting to up to almost 300% due to flip angle variation across the slice. A non-constant divergent signal for SPGR-VFA with hyperpolarized samples is often interpreted as a consequence of imperfect flip angle

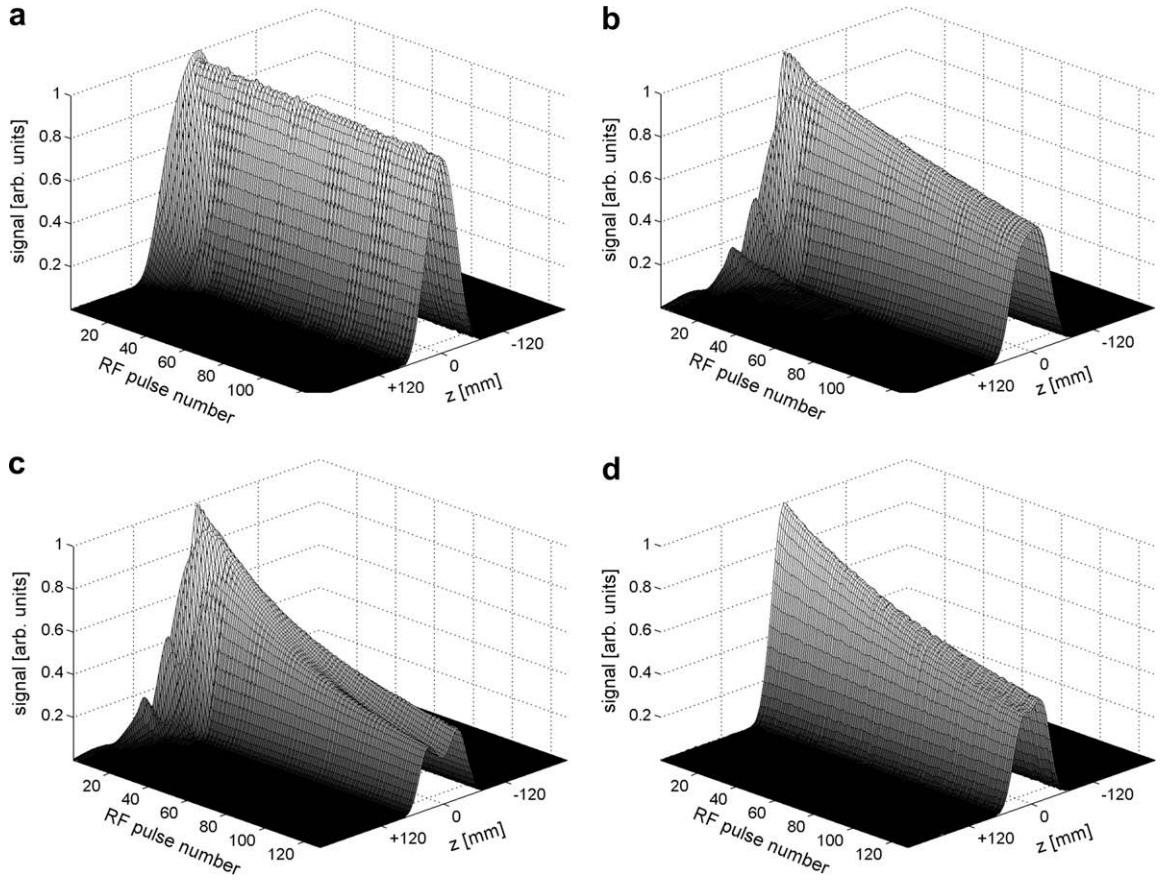

Fig. 7. Evolution of slice profiles in a balanced SSFP sequence for flip angles of (a) 14°, (b) 42°, and (c) 70°. For comparison, (d) shows the reference case of SPGR-CFA with a flip angle of 7°.

calibration and B_1 transmit coil inhomogeneity. While this is certainly the case for 3D sequences [2] and 2D projection imaging with a very weak or absent slice selection gradient [11,18], this work demonstrates that the effect is inherent to slice-selective 2D imaging by virtue of flip angle variation across the slice.

The simplest approach to improve the slice profile and *k*-space filtering performance of the SPGR-VFA sequence is to discard the later RF views. This could be done prospectively, by using Eq. (1) to calculate the flip angle progression, replacing the total number of RF pulses N by $N + M$, where M is an integer number of additional 'discarded' pulses. Thus, the flip angle progression is calculated for a higher number of pulses than are actually played out.

This would mean that not all of the available magnetization is used, and hence this method is slightly less efficient than the ideal progression according to Eq. (1); however, for a small number of discarded pulses the difference in signal is relatively small. As the transverse magnetization is kept constant during the imaging experiment, the size of the signal is determined by the flip angle of the first RF pulse. For example, considering an experiment in which 128 phase encode views are to be acquired, the initial flip angle is reduced from 5.07° to 4.88° if the calculation is done for 138 views, which corresponds to ten discarded views. This is equivalent to a signal loss of less than 4%. Nevertheless, depending on the RF pulse shape as shown in Fig. 3e, the deviation from a flat *k*-space filter can be as much as 10% as early as after the 60th RF pulse, and a flat filter might necessitate the discarding of a large number of RF views.

The most comprehensive solution to this problem would be a dynamic modification of the RF pulse shape from view to view [14], which is intensive in terms of spectrometer run time memory usage. An alternative method which is somewhat easier to implement is proposed in this work. Slice selection gradient scaling as a function of RF pulse number results in a satisfactory *k*-space filter, while a constant signal is maintained in the slice center. Nevertheless, the shape of the observed slice profile for later pulses still deviates from the ideal profile.

Obviously the amount of correction depends on the pulse shape, with higher RF bandwidth pulses (for a given pulse duration) requiring less correction. This can also be seen in Fig. 4b, where the correction factor is smaller for higher RF bandwidth pulses. From this perspective the use of pulses with a large time–bandwidth product can be regarded as preferable, bearing in mind that it might be necessary to skip the last few RF views. Particularly for high RF bandwidth the use of 90° pulses at the end of an imaging sequence can lead to the highly undesirable excess signal in sidebands outside of the slice as seen in Figs. 3 and 5b and c.

There is, however, a number of arguments in favor of RF pulses with a smaller time–bandwidth product, particularly for imaging of hyperpolarized ^{3}He. By using lower bandwidth pulses, the same slice thickness can be achieved for a weaker slice selection gradient, which reduces diffusion attenuation during slice selection [12]. Alternatively, for a given slice gradient strength lower TEs can be attained. Additionally, lower bandwidth pulses deliver higher flip angles for lower RF transmit power, which might become important for nuclei of lower gyromagnetic ratio with body transmit coils and limited broadband RF amplifier power. Ultimately the choice of RF pulse is determined by the nature of the imaging experiment; however, the effects described in this work should be taken into account when designing 2D experiments on hyperpolarized nuclei.

The correction mechanism based on slice gradient scaling proposed here is based on knowledge of the uncorrected slice profile evolution. This knowledge can either be obtained by a preparation measurement or by simulation. An additional measurement, requiring an additional dose of hyperpolarized agent, is not very practical for in vivo studies, given the overhead in scanning time and the relatively large additional amount of agent needed.

An advantage of slice profile correction based on a preliminary measurement is that it corrects not only for the flip angle variation inherent to the excitation pulse shape, but also takes into account the B_1 inhomogeneity of the transmit coil across the excited slice and polarization mixing due to gas diffusion through the slice [12]. This is a consequence of the fact that all calculations are carried out in the spatial rather than the temporal domain. For in vivo studies, however, both of these effects are expected to be reduced, as usually good B_1 homogeneity can be reached on the scale of a typical slice thickness [19], and in vivo diffusion is reduced considerably by the structure of the lung. Hence it can be assumed that, for in vivo studies, correction factors obtained from simulations would allow satisfactory correction of slice profile deviations.

In principle, the performance of a simulation-based correction approach is defined by the quality of the simulations. The effects of B_1 inhomogeneity and diffusion dephasing have not been incorporated in the simulations presented here. In the existing framework, the correction factors obtained from simulations are expected to perform best if the transmit field is homogeneous and diffusion dephasing is minimized. The results shown in Fig. 6 demonstrate good correction performance for a Gaussian RF pulse. If a pulse with larger bandwidth is used, the slice gradient becomes stronger, exacerbating diffusion dephasing. This effect could, however, be readily accounted for within the framework of the simulations using the approach outlined in [12].

For simplicity, the present experiments were limited to a single slice. In multi-slice imaging the situation is somewhat more complex. Signal at the slice edge would be expected to be reduced if longitudinal magnetization in the adjacent slice has been depleted by previous pulses. Depending on the order in which slices are acquired this might result in asymmetric slice profiles. This effect could be mitigated by slice interleaving as this would lead to a more uniform depletion of longitudinal magnetization across all slices. Of course, a viable alternative for imaging whole objects avoiding these issues is presented by 3D sequences, which benefit from the fact that a long TR is not necessary (and, in fact, undesirable) for hyperpolarized nuclei [12]. Under certain circumstances it might, however, be desired to acquire only a subset of slices, in which case aforementioned effects might have to be considered.

Particularly in hyperpolarized noble gas imaging diffusion plays an important role. Two different diffusion mechanisms along the direction of slice selection have an influence on the data presented here. Diffusion of transverse magnetization during TE leads to a broadening of the slice profile, as spins move between excitation and detection, and diffusion of longitudinal magnetization between pulses leads to partial replenishment of the depleted polarization.

Assuming a diffusion coefficient of $D = 0.9\ \mathrm{cm^2\ s^{-1}}$ for ^{3}He in N_2, the diffusion length during TE = 4.2 ms is 1.2 mm. This gives an estimate for the size of the first effect in the present experiments. Even using a very diffusive gas such as pure ^{3}He and a rather long TE, the expected broadening is small compared to typical slice thicknesses in 2D imaging. Here the gas was freely diffusive within the phantom. In in vivo lung imaging, the effect of diffusion during TE will be even less pronounced due to the presence of restrictions.

Diffusion of longitudinal magnetization between pulses plays a more significant role in the present experiments. This effect has been modeled and measured previously for the 2D experiment with free gas with finite difference simulations [12]. As long as the compensation strategy proposed is based on experimental data, these effects are inherently taken into account. Nevertheless, occasional misalignment of the phantom led to the presence of gas reservoirs of different volumes on both sides of the imaged slice. This resulted in asymmetric slice profiles for later RF pulses, as replacement of depleted polarization was more efficient from the larger reservoir. An example for this effect can be seen in Fig. 7d, where the observed slice profiles exhibit a slight asymmetry for later RF pulses.

In addition to the insights gained in this work on slice-selective SPGR-VFA imaging, a balanced 2D SSFP sequence was also evaluated with respect to slice profile effects in hyperpolarized MRI. It was found that, in comparison to SPGR-CFA with equivalent flip angle, the slice profile is better conserved using a SSFP sequence, as RF depletion is reduced due to rephasing of transverse magnetization by balanced gradients. This is a new finding, as previous studies with SSFP in hyperpolarized imaging have focused on the analysis of magnetization evolution in the k_y direction, motivated by the possibility of using higher flip angles, resulting in higher SNR [8]. Together with the results obtained here for SPGR-VFA, SSFP with relatively small flip angles ($<20^\circ$) might be considered as an alternative to SPGR-VFA for minimizing image blurring, particularly in 2D slice-selective imaging.

The usefulness to this end of the SSFP sequence used here is limited, however, as additional slice profile distortions are observed in the first $\sim$20 RF pulses. These arise from the frequency distribution of spins as a consequence of B_0 imperfection. These off-resonance spins accrue additional phase between RF pulses, which leads to oscillating signal behavior until their spin coherence has completely dephased. The performance of SSFP could be improved further by better tailored start-up schemes to catalyze the equilibrium magnetization and reduce oscillating behavior before acquisition, along the lines of methods proposed to accelerate the transition into the steady state in ^{1}H MRI [20,21]. The investigation of such schemes for SSFP of hyperpolarized nuclei will be the subject of future experiments.

All SSFP acquisitions presented here were done using on-resonance RF excitation. Off-resonance excitation is known to lead to significant slice profile distortions in balanced SSFP imaging [22]; however, a detailed investigation of the influence of deliberate off-resonance excitation is beyond the scope of this work.

The magnetic environment during in vivo imaging is more heterogeneous compared to the phantom experiments shown here, as tissue susceptibility plays a role. In SSFP imaging this increases both the transient oscillations in the initial phase of the experiment and the banding artifacts arising in areas of low B_0 homogeneity. Hence every effort should be made to minimize TR in SSFP, to which end RF pulses of lower bandwidth again become interesting. Ultimately the usefulness of SSFP sequences in general is greater in systems with strong gradients and fast slew rates for the same reason.

In conclusion, slice profile effects were investigated in 2D slice-selective SPGR-VFA and balanced SSFP imaging of hyperpolarized ^{3}He. It was shown that in SPGR-VFA the distribution of flip angles across the slice results in large excess signal from the slice edges in later RF pulses, which in turn leads to non-constant transverse magnetization. A correction mechanism for this effect via scaling of the slice gradient was proposed. Furthermore it was demonstrated that SSFP imaging using small flip angles results in a better preservation of the slice profile than SPGR sequences.

Funding

EU Framework VI Programme, Phelinet.
EPSRC # EP/D070252/1, EPSRC Doctoral Training Award
GE Healthcare for polarizer support

References

[1] J.M. Wild, M.N.J. Paley, L. Kasuboski, A. Swift, S. Fichele, N. Woodhouse, P.D. Griffiths, E.J.R. van Beek, Dynamic radial projection MRI of inhaled hyperpolarized ^{3}He gas, Magn. Reson. Med. 49 (2003) 991–997.

[2] J.H. Holmes, R.L. O'Halloran, E.K. Brodsky, Y. Jung, W.F. Block, S.B. Fain, 3D hyperpolarized He-3 MRI of ventilation using a multi-echo projection acquisition, Magn. Reson. Med. 59 (2008) 1062–1071.

[3] M. Salerno, T.A. Altes, J.R. Brookeman, E.E. de Lange, J.P. Mugler III, Dynamic spiral MRI of pulmonary gas flow using hyperpolarized ^{3}He: preliminary studies in healthy and diseased lungs, Magn. Reson. Med. 46 (2001) 667–677.

[4] A. Haase, J. Frahm, D. Matthaei, W. Hänicke, K.-D. Merboldt, FLASH imaging: rapid NMR imaging using low flip-angle pulses, J. Magn. Reson. 67 (1986) 258–266.

[5] H.Y. Carr, Steady-state free precession in nuclear magnetic resonance, Phys. Rev. 112 (1958) 1693–1701.

[6] A. Oppelt, R. Graumann, H. Barfuss, H. Fischer, W. Hertl, W. Schajor, FISP: a new fast MRI sequence, Electromedica 54 (1986) 15–18.

[7] K. Scheffler, S. Lehnhardt, Principles and applications of balanced SSFP techniques, Eur. Radiol. 13 (2003) 2409–2418.

[8] J.M. Wild, K. Teh, N. Woodhouse, M.N.J. Paley, S. Fichele, N. de Zanche, L. Kasuboski, Steady-state free precession with hyperpolarized ^{3}He: experiments and theory, J. Magn. Reson. 183 (2006) 13–24.

[9] J.M. Wild, M.N.J. Paley, M. Viallon, W.G. Schreiber, E.J.R. van Beek, P.D. Griffiths, *K*-Space filtering in 2D gradient-echo breath-hold hyperpolarized ^{3}He MRI: spatial resolution and signal-to-noise ratio considerations, Magn. Reson. Med. 47 (2002) 687–695.

[10] E.M. Haacke, R.W. Brown, M.R. Thompson, R. Venkatesan, Magnetic Resonance Imaging, Physical Principals and Sequence Design, Wiley-Liss, New York, 1999. pp. 463–465.

[11] L. Zhao, R. Mulkern, C.H. Tseng, D. Williamson, S. Patz, R. Kraft, R.L. Walsworth, F.A. Jolesz, M.S. Albert, Gradient-echo imaging considerations for hyperpolarized ^{129}Xe MR, J. Magn. Reson. B 113 (1996) 179–183.

[12] J.M. Wild, N. Woodhouse, M.N.J. Paley, S. Fichele, Z. Said, L. Kasuboski, E.J.R. van Beek, Comparison between 2D and 3D gradient-echo sequences for MRI of human lung ventilation with hyperpolarized ^{3}He, Magn. Reson. Med. 52 (2004) 673–678.

[13] J.M. Pauly, P. Le Roux, D. Nishimura, A. Macovski, Parameter relations for the Shinnar-Leroux selective excitation pulse design algorithm, IEEE T. Med. Imaging 10 (1991) 53–65.

[14] A.B. Kerr, J.M. Pauly, Slice profile stabilization for segmented *k*-space magnetic resonance imaging, United States Patent 5,499,629, 1996.

[15] K. Teh, N. de Zanche, J.M. Wild, Radiation-damping effects in a birdcage resonator with hyperpolarized He-3 gas at 1.5 T, J. Magn. Reson. 185 (2007) 164–172.

[16] E.X. Wu, R.B. Buxton, Effect of diffusion on the steady-state magnetization with pulsed field gradients, J. Magn. Reson. 90 (1990) 243–253.

[17] M. Deimling, O. Heid, Magnetization prepared True FISP imaging, Proc. Int. Soc. Magn. Reson. Med. 2 (1994) 495.

[18] G.E. Santyr, W.W. Lam, A. Ouriadov, Rapid and efficient mapping of regional ventilation in the rat lung using hyperpolarized ^{3}He with flip angle variation for offset of RF and relaxation (FAVOR), Magn. Reson. Med. 59 (2008) 1304–1310.

[19] N. de Zanche, N. Chhina, K. Teh, C. Randell, K.P. Pruessmann, J.M. Wild, Asymmetric quadrature split birdcage coil for hyperpolarized ^{3}He lung MRI at 1.5 T, Magn. Reson. Med. 60 (2008) 431–438.

[20] B.A. Hargreaves, S.S. Vasanawala, J.M. Pauly, D.G. Nishimura, Characterization and reduction of the transient response in steady-state MR imaging, Magn. Reson. Med. 46 (2001) 149–158.

[21] J. Hennig, O. Speck, K. Scheffler, Optimization of signal behavior in the transition to driven equilibrium in steady-state free precession sequences, Magn. Reson. Med. 48 (2002) 801–809.

[22] F. Staehle, J. Leupold, J. Hennig, M. Markl, Off-resonance-dependent slice profile effects in balanced steady state free precession imaging, Magn. Reson. Med. 59 (2008) 1197–1202.